Ocean Modelling 95 (2015) 38–52

Contents lists available at ScienceDirect

Ocean Modelling

journal homepage: www.elsevier.com/locate/ocemod

The effect of basal friction on melting and freezing in ice shelf–ocean models

David E. Gwyther[a,b,*], Benjamin K. Galton-Fenzi[c,b], Michael S. Dinniman[d], Jason L. Roberts[c,b], John R. Hunter[b]

[a] Institute for Marine and Antarctic Studies, University of Tasmania, Private Bag 129, Hobart, Tasmania 7001, Australia
[b] Antarctic Climate & Ecosystems Cooperative Research Centre, University of Tasmania, Private Bag 80, Hobart, Tasmania 7001, Australia
[c] Australian Antarctic Division, Channel Highway, Kingston, Tasmania 7050, Australia
[d] Center for Coastal Physical Oceanography, Old Dominion University, Norfolk, Virginia, USA

ARTICLE INFO

Article history:
Received 4 March 2015
Revised 17 September 2015
Accepted 20 September 2015
Available online 30 September 2015

Keywords:
Ice shelf–ocean interaction
Basal roughness
Melt/freeze parameterisation
Drag and friction
Melt plume
Antarctic mass loss

ABSTRACT

The ocean is an important control on the mass budget of the Antarctic ice sheet, through basal melting and refreezing underneath the floating extensions of the ice sheet known as ice shelves. The effect of the ice surface roughness (basal roughness) on melting and refreezing is investigated with idealised ice shelf–ocean numerical simulations. Both "hot" ocean forcing (e.g. Pine Island Glacier; high basal melting) and "cold" ocean forcing (e.g. Amery Ice Shelf; low basal melting, stronger refreezing) environments are investigated. The interaction between the ocean and ice shelf is further explored by examining the contributions to melt from heat exchange across the ice–ocean interface and across the boundary layer–ocean interior, with a varying drag coefficient. Simulations show increasing drag strengthens melting. Refreezing increases with drag in the cold cavity environment, while in the hot cavity environment, refreezing is small in areal extent and decreases with drag. Furthermore, melting will likely be focussed where there are strong boundary layer currents, rather than at the deep grounding line. The magnitude of the thermal driving of the basal melt decreases with increasing drag, except for in cold cavity refreeze zones where it increases. The friction velocity, a function of the upper layer ocean velocity and the drag coefficient, monotonically increases with drag. We find friction-driven mixing into the boundary layer is important for representing the magnitude and distribution of refreezing and without this effect, refreezing is underestimated. Including a spatially- and temporally-varying basal roughness (that includes a more realistic, rougher refreezing drag coefficient) alters circulation patterns and heat and salt transport. This leads to increased refreezing, altered melt magnitude and distribution, and a pattern of altered vertical flow across the entire ice shelf. These results represent a summary of melting and freezing beneath ice shelves and strongly motivate the inclusion of appropriate vertical mixing schemes and basal roughness values that vary spatially and temporally in ocean models of ice shelf cavities.

1. Ice shelf basal roughness

Ice shelves form around the Antarctic coastline where the ice sheet flows into the ocean. Hydrostatic pressure from the ocean lifts the ice off the bedrock at the 'grounding line', forming an ice shelf and ocean-filled cavity beneath (see Fig. 1(a and b)). The flow of the ice sheet into the ocean is controlled in part by the buttressing effect of ice shelves (Paterson, 2002; Dupont and Alley, 2005). Understanding the dynamics and mass loss from ice shelves is important for projecting future ice sheet flow and Antarctic mass balance (Pritchard et al., 2012).

Approximately half of the mass loss from the Antarctic Ice Sheet is from basal melting (1454 ± 174 Gt/yr. Depoorter et al., 2013), where warm (relative to the local pressure freezing point) ocean temperatures drive melting at the base of ice shelves. Increases in the rate of thinning of Antarctic ice shelves attributed to increased basal melting (Pritchard et al., 2012) suggests increased heat delivery to sub-ice shelf cavities. There are several different mechanisms hypothesised to be increasing the delivery of warmer water to ice shelf cavities, including changing wind regimes (Dinniman et al., 2012), polynya and sea ice interactions (Holland et al., 2010; Cougnon et al., 2013; Gwyther et al., 2014), thermocline shoaling (Hattermann et al., 2014) and coastal current redirection

* Corresponding author at: Institute for Marine and Antarctic Studies, University of Tasmania, Private Bag 129, Hobart, Tasmania 7001, Australia.
E-mail address: david.gwyther@gmail.com (D.E. Gwyther).

http://dx.doi.org/10.1016/j.ocemod.2015.09.004
1463-5003/

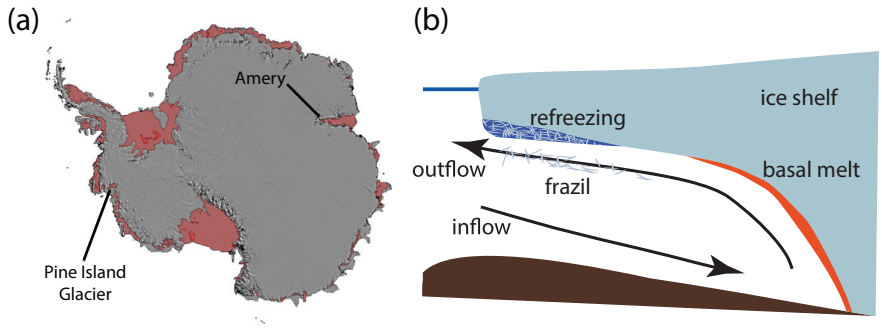

Fig. 1. (a) Antarctic ice shelves, including Pine Island Glacier Ice Shelf and Amery Ice Shelf, are marked in red on a MODIS MOA basemap (Scambos et al., 2007; Greene et al., 2013). (b) The ice shelf environment is illustrated, showing the grounding line, ocean inflow and outflow, basal melting and refreezing. (For interpretation of the references to colour in this figure legend, the reader is referred to the web version of this article.)

(Jacobs et al., 2011; Hellmer et al., 2012). The plethora of different driving mechanisms suggests regionally-varying factors are important for controlling delivery of oceanic heat.

Basal melting at the ice-ocean interface is a function of the ocean circulation and amount of heat within the boundary layer, which can be subdivided into three layers. Direct interaction between the flow and the surface roughness occurs in the viscous sublayer, where molecular viscous forces are dominant ($\mathcal{O}(1)$ cm thick; Soulsby, 1983). This lies within the logarithmic layer (log layer; $\mathcal{O}(1)$ m), where the vertical velocity profile can generally be described with a simple logarithmic relationship or 'law of the wall' (Soulsby, 1983). Together with the outer layer (extending out to $\mathcal{O}(10)$ m; Soulsby, 1983), which is most influenced by the free-stream flow, these comprise the boundary layer. Heat and salt enter the boundary layer from the ocean below and mixing carries heat and salt to the ice interface. Basal roughness controls the turbulent exchange of heat to the ice–ocean interface and changes the thickness of the boundary layer (which affects entrainment and delivery of heat from below). Basal melting is also a function of hydrostatic pressure (through the pressure dependence of the freezing point temperature), ice shelf basal slope (through the velocity and thickness of the buoyant boundary layer) and driving temperature (Holland et al., 2008).

Using observations of the boundary layer shear profile to determine the coefficient of drag (C_D) has only been accomplished beneath relatively thin sea ice (McPhee et al., 1987; McPhee, 1992) but it is likely that this environment is different from the sub-ice shelf environment. Nevertheless, values of C_D used for the ice shelf–ocean interface in various numerical studies typically range between $C_D = 0.0015$ (e.g. Millgate et al., 2013), $C_D = 0.0025$ (e.g. Hunter, 2006; De Rydt et al., 2014) or $C_D = 0.003$ (e.g. Timmermann, 2002; Dinniman et al., 2007; Klinck and Dinniman, 2010). As C_D is the least observed parameter, it is often tuned to reduce the mismatch between the simulated and observed melt rates (e.g. Jenkins et al., 2010). However, all ice shelf–ocean models to date have used a single C_D for the entire ice–ocean interface, where in reality C_D will vary both spatially and temporally. It is likely that C_D would vary between zones of melting (where ablation of ice would lead to a hydraulically smoother interface and low C_D) and refreezing (high C_D due to the porous and flaky nature of marine-accreted ice (Craven et al., 2009)).

The roughness of the ice shelf-ocean interface affects melting at two different levels; by affecting turbulent flux of heat across the ice shelf-ocean interface (Section 1.1), and by changing the shear profile, boundary layer thickness and consequently entrainment of heat into the boundary layer (Section 1.2).

1.1. Ice–ocean heat flux

The roughness of the ice shelf interface affects basal melting by influencing the transfer of heat (and salt) via turbulence, across the ice shelf-ocean interface, as in Fig. 2. Most ocean models use a simple '3-equation parameterisation' of the ice-ocean interface (Hellmer and Olbers, 1989; Scheduikat and Olbers, 1990; Holland and Jenkins, 1999). See Appendix A for details.

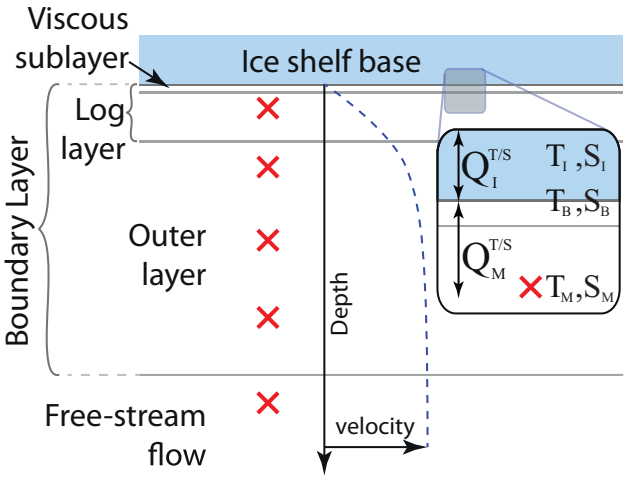

Fig. 2. The ice shelf–ocean interface is illustrated, with a vertical velocity profile (blue dashed line) and example model grid points (red crosses). Inset shows the ice shelf–ocean interface with temperature (T), salinity (S), heat flux (Q^T) and salt flux (Q^S) shown. Subscripts I, B and M refer to the ice shelf, ice shelf base and ocean model top cell, respectively. (For interpretation of the references to colour in this figure legend, the reader is referred to the web version of this article.)

In the Holland and Jenkins (1999) parameterisation, T_M and S_M refer to the mixed layer temperature and salinity. Defining a mixed layer of a single density class below the ice shelf interface is appropriate in an isopycnal coordinate model (e.g. Holland and Jenkins, 2001). However, we define the ice shelf–ocean interface in terms of the momentum boundary layer, which is critical for transferring the temperature and salinity properties from the interior cavity to the ice shelf. To implement the parameterisation, it is standard practice to use the values of T and S in the top model cell (e.g. Dansereau et al., 2014). However, as we are able to resolve the outer layer explicitly, T_M and S_M taken from the upper-most model cells are within the log layer, rather than from the outer layer. Therefore models that resolve $\leq\mathcal{O}(1)$ m at the ice shelf–ocean interface may provide different estimates of the gradients of temperature and salinity across the boundary layer and hence, different melt rates. However, a large proportion of the temperature and salinity changes occur over the viscous sublayer, which can lead to relatively well-mixed conditions through the rest of the boundary layer (Steele et al., 1989). In such cases, the standard practice for implementing the Holland and Jenkins (1999) parameterisation will produce results approximately consistent with

observations (Jenkins et al., 2010). The standard practice for implementation of T_M and S_M utilised here is useful for the comparative nature of this study, but does warrant future investigation, particularly as model vertical resolution increases and the top model cell reduces in thickness. Note that we maintain the M subscript for consistency.

Turbulence is generated by velocity shear through the boundary layer. It is convenient to define the shear stress at the interface in terms of the friction velocity, $\tau_0 = \rho u_*^2$, where ρ is density and u_* is the friction velocity. In these experiments, there is a lower limit on friction velocity, $u_{*,min} = 2 \times 10^{-5}$ m s^{-1}, which is chosen to represent heat transfer by molecular diffusion alone. The presence of turbulence inhibits the direct description of the shear stress and mean flow relationship, and hence we must introduce a parameterisation. We assume a quadratic relationship between shear stress and mean flow, $\tau_0 = \rho C_D U_M^2$, where U_M is the mean flow in the boundary layer, yielding a relationship between the mean boundary layer flow and the friction velocity,

$$u_* = \sqrt{C_D}|U_M|, \tag{1}$$

where C_D is a nondimensional drag coefficient. Note that since this is a parameterisation of the non-resolved layers between the top model grid point and the interface, it is understood to have an implicit depth dependence. It follows that changes in vertical resolution will impact the choice of C_D in ocean models.

The three coupled thermodynamic equations (Eqs. A.1–A.3) govern the thermal regime of the boundary layer and can be simultaneously solved, yielding the melt rate at the ice shelf base, m, and the temperature and salinity of the seawater in contact with the base of the ice, T_B and S_B, respectively. An expression for m is given by rearranging Eq. A.2 and substituting the expression for the latent heat flux and heat conduction into the ice,

$$m = -\frac{c_{p,M}}{L_f}\gamma_T(T_B - T_M) + \frac{\rho_I}{\rho_M L_f}\alpha_I^T \left.\frac{\partial T_I}{\partial z}\right|_B. \tag{2}$$

The first term on the right hand side of Eq. 2 is the melting due to the thermal driving (difference between the interface temperature, T_B and the log layer temperature, T_M) and the thermal exchange velocity γ_T (which is a function of u_*), where $c_{p,M}$ is the log layer specific heat capacity, and L_f is the latent heat of fusion. The second term on the RHS is a reduction of melting due to heat conduction into the ice shelf, where ρ_I is the mean ice density, ρ_M is the log layer density, α_I^T is the thermal diffusivity of ice and $\frac{\partial T_I}{\partial z}|_B$ is the ice shelf vertical temperature gradient evaluated at the base of the ice shelf. There is an analogous equation for melt rate derived from the salt balance at the ice–ocean interface, which depends on the salt exchange velocity (γ_S; also a function of u_*) and the salinity difference at the interface, obtained by rearranging Eq. A.3. Note that throughout this paper, the exchange velocities, γ_T and γ_S are referred to as $\gamma_{T|S}$ for brevity.

In the implementation of the three equation parameterisation, both of these equations are utilised to solve for m, and as such, it is a function of both the temperature and salinity difference from the interface to the log layer. As the heat conduction term of Eq. 2 is small compared to the melting, then we see that m is primarily dependent on the exchange velocities (which are a function of circulation and roughness) and the thermal driving. In the model, heat conduction into the ice is captured with a vertical diffusion and advection scheme (see Holland and Jenkins, 1999) which modifies melting and freezing at the ice shelf–ocean interface.

1.2. Friction-driven turbulent mixing

Turbulent mixing of interior waters into the boundary layer is controlled by the friction velocity, u_*, which impacts both the mixing and entrainment rate of heat and salt and thickness of the boundary layer (see Fig. 2). Consequently, C_D (see Eq. 1) affects the mixing of heat into the boundary layer, and thus changes the thermal driving of the melting and freezing.

Vertical mixing in this study is simulated using the scheme outlined in Large et al. (1994), hereinafter referred to as LMD94. LMD94 splits mixing into interior oceanic mixing (comprised of vertical diffusivities resulting from shear instability, internal wave mixing and double diffusivity) and boundary layer mixing. LMD94 parameterise boundary layer mixing with a vertical profile of eddy diffusivity, K_x (where x represents momentum, salinity or temperature). The eddy diffusivity is used to calculate the kinematic flux (transport of a variable per unit time), $-K_x \frac{\partial X}{\partial z}$, where z is the upward vertical coordinate, and X is the time average of property x. Importantly, the eddy diffusivity and thus vertical flux, scales with the thickness of the boundary layer, h, via $K_x(\sigma) = h w_x(\sigma) G(\sigma)$, where $\sigma = d/h$ is a dimensionless vertical coordinate (varying from 0 to 1) indicating fractional position in the boundary layer, $G(\sigma)$ is a nondimensional cubic polynomial 'shape function', $w_x(\sigma)$ is the turbulent velocity scale and d is the distance coordinate from the ice-ocean boundary.

Boundary layer thickness in LMD94 depends on the surface forcing (beneath an ice shelf the forcing is due to momentum stress from basal roughness and a buoyancy flux of salt and heat due to melting or freezing) and is estimated with a bulk Richardson number ($Ri_b(d)$) describing the ratio of the stabilising effect of buoyant stratification (buoyancy profile is $B(d)$) to the destabilising effect of velocity shear (shear profile is $\vec{v}(d)$),

$$Ri_b(d) = \frac{(B_r - B(d))d}{|\vec{V}_r - \vec{V}(d)|^2 + \vec{V}_t^2(d)}. \tag{3}$$

Here, $\vec{V}_r$ and B_r are the average velocity and buoyancy where Monin–Obukhov similarity theory applies (assumed to be ~0.1 of the boundary layer thickness), while $\vec{V}_t(d)$ is the turbulent velocity profile. The boundary layer thickness is equated to the smallest value of d such that $Ri_b(d) = Ri_c$, where $Ri_c = 0.3$ is a critical Richardson number. Physically, eddies (with buoyancy and velocity corresponding to conditions at the viscous sublayer) will only be able to intrude to a depth of h, at which point they will become stable relative to the local buoyancy and velocity. As a result, a thicker boundary layer will be able to contain larger eddies and hence more energetic eddy mixing. Consequently, as basal roughness (and circulation) controls the velocity shear profile across the boundary layer, so the boundary layer thickness will increase with increasing C_D.

1.3. Geophysical considerations

The ice shelf cavity environment commonly falls into one of two classifications: 'cold cavity' and 'hot cavity', referring to the relative characteristics of the inflow water (Joughin et al., 2012). A 'cold cavity' scenario occurs where relatively cold water, often produced during sea ice formation (for example High Salinity Shelf Water (HSSW) with a temperature of ~ −1.9°C and salinity of 34.7 on the Practical Salinity Scale), enters the ice shelf cavity, resulting in low melt rates (typically an area average below ~1 m/yr). A typical example is the Amery Ice Shelf cavity, thought to be dominated primarily by HSSW (Galton-Fenzi et al., 2012) and Ice Shelf Water below the surface freezing point (Herraiz-Borreguero et al., 2013). In this environment, melting is weak (typically 0.74 m ice/yr; Galton-Fenzi et al., 2012). As the sub-ice shelf water temperature in these environments is relatively cold, the injection of cold meltwater can result in supercooling below the in situ freezing point and frazil crystal formation with significant refreezing regions. Furthermore, the 'ice pump' mechanism, whereby deep melting leads to a buoyant meltwater plume rising along the ice shelf base and (due to the pressure dependence of the freezing point of seawater) refreezing at a shallower point along the base (Lewis and Perkin, 1986), is strong in this situation. In contrast, the 'hot cavity' has relatively warm and saline inflow waters and higher

melting such as for Pine Island Glacier Ice Shelf. In this example, Circumpolar Deep Water (at temperatures >0.5 °C and salinity of 34.6; >3.5 °C above the in situ freezing point) enters the ice shelf cavity, leading to strong melting. Hydrography-based estimates of melt rate are 22 − 33 m/yr(Jacobs et al., 2011), while glaciological estimates are 47 m/yr over the inner 1005 km^2 of the ice shelf and 84 m/yr closer to the grounding line (Warner and Roberts, 2013). In this situation, the warm environment diminishes the role of refreezing in the 'ice pump', but strengthens the buoyancy-driven circulation. The importance of these cavity environments for driving melt rate, the regional differences, and the generally unexplored nature of the fundamentals of ice shelf–ocean interaction motivate the study of the details of both environments.

1.4. Study scope

This study comprises numerical simulations investigating:

- the effect of C_D on the melt/freeze rate, circulation and oceanic boundary layer properties,
- the relative importance of C_D on driving heat flux into the ice interface and on mixing heat into the boundary layer,
- the effect of spatially- and temporally-varying C_D on melt/freeze, circulation and oceanic boundary layer properties, compared to a commonly chosen constant basal roughness value.

We provide an overview of the role of basal roughness in modifying and controlling melting and freezing in an ice shelf–ocean model containing either hot or cold cavities and inform the choice of C_D in the parameterisation of the ice–ocean interface and boundary layer environment. We show the need to include a realistic, spatially-varying basal roughness parameter in future ice shelf–ocean models.

2. Model setup

A modified version of the Regional Ocean Modelling System (ROMS; Shchepetkin and McWilliams, 2005), a 3-D primitive equation finite difference ocean model, was used to simulate ice shelf–ocean interaction. The modifications include the addition of thermodynamic interaction between ocean and the ice shelf (see Dinniman et al., 2007; Galton-Fenzi et al., 2012). ROMS has been shown to be able to handle the steep change in water column thickness at the ice shelf front through many ice shelf–ocean modelling studies (Dinniman et al., 2007; Galton-fenzi, 2009; Galton-Fenzi et al., 2012; Mueller et al., 2012; Cougnon et al., 2013; St-Laurent et al., 2013; Gwyther et al., 2014, and others).

The model domain is designed to simulate an ice shelf and extends from 0°E to 15°E, 70°S to 80°S, with a linearly southward downsloping ice draft (starting at 200 m at 76°S and deepening to 700 m at 80°S), and a flat bathymetry (900 m). The geometry shown in Fig. 3 is the Ice Shelf–Ocean Model Intercomparison Project (ISOMIP) geometry 2 (Hunter, 2006). We chose a linearly sloping ice draft as it is the standard geometry for investigating idealised ice shelf–ocean interaction. Using this ice shelf geometry allows intercomparison with recent studies that also employ the same ice shelf geometry (Dansereau et al., 2014). Furthermore, Holland et al. (2008) found a non-linear ice shelf shape produces weaker melting on average, but has the same quadratic relationship between melting and thermal driving as a linearly sloping ice shelf draft. While Little et al. (2009) found a departure from this quadratic dependence of melt rate on thermal driving with different ice shelf geometries, all of their geometries showed a common super-linear response to increasing ocean temperature. As we are more interested in the melt relationships rather than the magnitude of melting, the results of this study should be applicable across more complex geometries.

The model is initialised with water of temperature −1.9°C and salinity of 34.4, following ISOMIP. The model has horizontal grid resolution of approximately 0.3° in the zonal direction and 0.1° in the meridional direction. ROMS uses a terrain-following vertical coordinate and the 24 vertical levels have an approximately sigmoidal distribution of vertical position, enhancing vertical resolution near the upper and lower surfaces. Cell thicknesses for the upper and lowest cell are ∼0.007 and ∼0.02 of the water column thickness respectively, and ∼0.078 of the water column thickness at mid-column depth. Thus, the centre of the top cell is ∼2 m from the bottom of the ice at the ice front, and ∼0.7 m from the bottom of the ice at the back of the cavity. The model is run for 30 years to approximate steady state, and the last year of output is averaged and used for analysis.

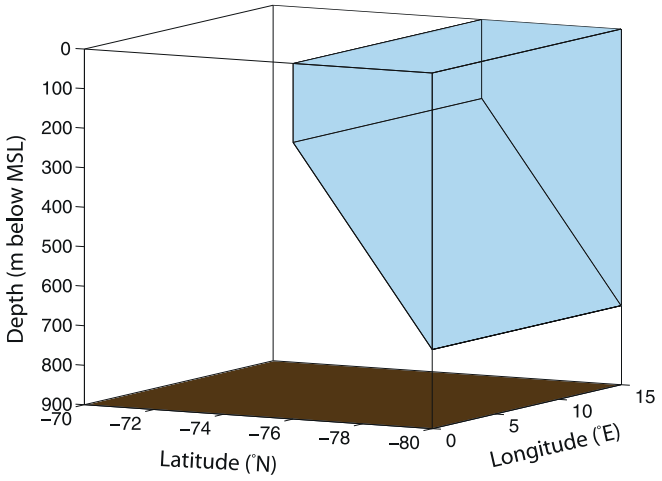

Fig. 3. Model geometry is shown from an oblique perspective, indicating the bottom bathymetry (brown) at 900 m below the surface, and ice surface (pale blue) linearly sloping down to 700 m with a 200 m thick ice front at 76°S. (For interpretation of the references to colour in this figure legend, the reader is referred to the web version of this article).

This experiment is designed to investigate ice shelf–ocean interaction in an idealised scenario by removing the obfuscating interaction of winds and inflowing ocean currents with sub-cavity water. As a result, circulation is controlled by the buoyancy forcing resulting from ice–ocean thermodynamics and the difference in buoyancy of the open ocean and sub-ice shelf environments. This is similar to previous ISOMIP-like experiments (Holland et al., 2008; Losch, 2008), where there are no forced inflow currents.

The lateral boundaries are treated as closed, leading to no heat or salt flow into the domain across any lateral boundary. Oceanic conditions within the model domain are restored through daily relaxation of the open ocean surface to constant temperature and salinity values. The surface forcing conditions are chosen to produce oceanic conditions within the ice shelf cavity similar to physical examples. For the cold cavity scenario, similar to Amery Ice Shelf, the open ocean surface is relaxed to −1.9°C and salinity of 34.5. The hot cavity scenario, similar to the Pine Island Glacier ice shelf cavity, is simulated by relaxing the open ocean surface temperature to 0.5°C and salinity to 34.6. Note that melt rates simulated in this environment will not be as high as if there was flow across the lateral boundaries.

Melting and freezing at the ice shelf–ocean interface (within the viscous sublayer) is simulated with the above mentioned three-equation parameterisation (Holland and Jenkins, 1999). Excepting the velocity-independent sensitivity studies (see Section 4.2), we employ velocity-dependent turbulent transfer velocities, which is important for capturing fluctuations in turbulence resulting from changes in flow (Jenkins et al., 2010). Mixing of heat and salt into the boundary layer from the ocean below is simulated with an eddy diffusivity parameterisation (Large et al., 1994). Both of these parameterisations have dependence on the drag coefficient, C_D.

Table 1
Summary of experiments showing the range of drag values and experiment conditions tested, such as whether $\gamma_{T/S}$ was a function of u_* (signified by a ✓) or was constant (×) and whether friction-driven turbulent mixing (FDTM) into the boundary layer was included (✓) or switched-off (×). Experiments in Section 3.1 are run with velocity-dependent $\gamma_{T/S}$ and with friction-driven turbulent mixing. Experiments in Sections 3.1 and 3.2 are repeated for both hot and cold cavity conditions, while Section 3.3 is run only under a cold cavity environment. The names of the control simulation run in Section 3.1 and the sensitivity simulations run in Section 3.2 are shown in the last column. Note the different C_D chosen for the cold and hot cavity sensitivity experiments in Section 3.2, and the control cases the results are compared against in Section 3.1.

	C_D	FDTM	$\gamma_{T/S}(u_*)$	Simulation name
Section 3.1	0.0005	✓	✓	Case a
	0.00075	✓	✓	
	0.001	✓	✓	
	0.003	✓	✓	
	0.005	✓	✓	
	0.006	✓	✓	
	0.009	✓	✓	
	0.01	✓	✓	
	0.05	✓	✓	Case a (hot)
	0.1	✓	✓	Case a (cold)
Section 3.2	0.0005	×	✓	Case b
	0.0005	✓	×	Case c
	0.0005	×	×	Case d
	0.1 (cold), 0.05 (hot)	×	✓	Case b
	0.05	✓	×	Case c
	0.05	×	×	Case d
Section 3.3	$C_{D,melt}$ / $C_{D,freeze}$	FDTM	$\gamma_{T/S}(u_*)$	
	0.003 / 0.01	✓	✓	
	0.003 / 0.1	✓	✓	

3. Experiments

This study is split up into three sets of experiments as follows, (1) spatially constant drag, (2) investigating the role of friction-driven turbulent mixing, and (3) spatially and temporally variable drag, which are discussed in turn.

3.1. Spatially constant drag

The first set of experiments investigate approximate steady state melting/freezing at the ice interface for a spatially constant C_D. The result is a suite of simulations over the range from smooth ice ($C_D = 0.0005$) through to rough ice ($C_D = 0.1$). Ten different values of C_D (Table 1) are repeated for two different forcing conditions; a cold cavity and hot cavity environment.

3.2. Velocity dependence/independence and friction-driven turbulence

Melting and freezing is dependent not only on u_* driving heat flow across the ice interface, but also the heat supply into the boundary layer. The friction-driven turbulent mixing of heat (a function of u_*) into the boundary layer drives the boundary layer temperature and salinity and therefore, thermal driving. This set of experiments will examine the melt dependence due to each contribution by examining four melt/freeze and boundary layer parametrisation cases, as follows:

(a) with velocity-dependent melting and friction-driven turbulent mixing
(b) with velocity-dependent melting and without friction-driven turbulent mixing
(c) without velocity-dependent melting and with friction-driven turbulent mixing
(d) without velocity-dependent melting and without friction-driven turbulent mixing.

The control run (case a) has both friction-driven turbulent mixing simulated through the boundary layer parameterisation; and turbulent heat and salt exchange velocities, $\gamma_{T/S}$, that vary as a function of C_D and u_*. Case (a) are those experiments done for Section 3.1. The first sensitivity study (case b) has the friction-driven mixing into the boundary layer switched-off, while $\gamma_{T/S}$ still varies as a function of u_*. The second sensitivity study (case c) has friction-driven mixing into the boundary layer simulated, but $\gamma_{T/S}$ are set to spatially constant values and not allowed to vary as a function of u_*, hence simulating velocity-independent melting. This is a similar experiment to that performed by Dansereau et al. (2014). The third sensitivity study (case d) has constant $\gamma_{T/S}$ and no friction-driven turbulent mixing.

Friction-driven turbulent mixing is nullified by turning off the u_* dependence in the LMD scheme, while the velocity-dependence in the calculation of melting and freezing is controlled by setting transfer coefficients $\gamma_{T/S}$ to constant values within the ice shelf thermodynamics code. The velocity-independent $\gamma_{T/S}$ values used in the case (c) experiments are determined by calculating the area-average $\gamma_{T/S}$ for the case (b) scenario with the same C_D. In this way, the exchange coefficients in the case (a) and case (b) simulations will be broadly similar, allowing exploration of the effect on the melt rate due to removing friction-driven turbulent mixing or spatial variation in $\gamma_{T/S}$.

We will then repeat these 3 cases for a low drag and high drag interface, and for a cold cavity and hot cavity scenario, leading to 12 model runs in total (Table 1).

3.3. Spatially- and temporally-varying drag

This set of experiments test the effect of spatially- and temporally-varying drag. This is achieved using a dynamic drag that varies spatially and temporally, depending on whether there is melting or freezing at the ice shelf–ocean interface (Table 1). For a cell that is melting, $C_D = 0.003$, to simulate the smooth ice interface while for a cell that is freezing, C_D is set to 0.01 or 0.1 to simulate rough marine ice. This 'dynamic drag' will be tested by running a simulation with melt/freeze dependent C_D until pseudo-steady state is achieved (30 years). The resultant melt rates at pseudo-steady state are compared to simulations with a spatially-constant drag appropriate for melting ($C_D = 0.003$), as in Section 3.1.

4. Results

4.1. Constant drag

In this section, we investigate the effect that the basal roughness parameter has on melting and oceanic boundary layer properties through the most common parameterisation of ice shelf–ocean interaction (Holland and Jenkins, 1999). Strong westwards flow and melting exists along the ice shelf front. For Figs. 5–8, the averaged value is calculated with (red) and without (black) the line of cells along the ice front. For this investigation, the dynamics over the majority of the ice shelf area are more important than that along the thin ice shelf front. Consequently, the reader should refer to the black markers, however the results including the ice front are included for completeness.

In a hot cavity with a commonly-used coefficient of drag ($C_D = 0.003$), melting occurs over the vast majority of the ice shelf area (Fig. 4); the eastern region of the ice shelf supports high melt rates as ocean water enters rapidly; melting is present but weaker for the rest of the ice shelf; excepting the deep south-eastern region where melting is driven by a large temperature differential (between inflowing water and the pressure melting point). The presence of melting over most of the ice shelf area results in large quantities of cold meltwater production which flows north-westwards under Coriolis and buoyancy forces. The north-western boundary is a refreeze zone,

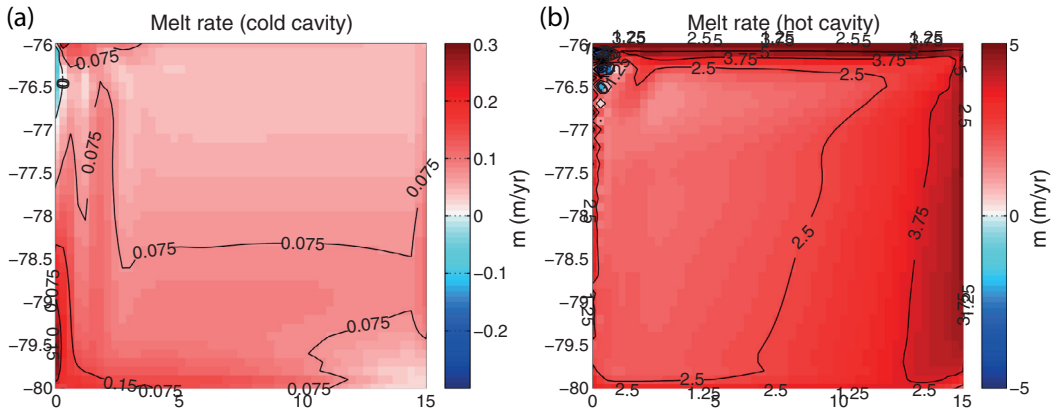

Fig. 4. Melt rate (positive for melting; negative for freezing) shown for (a) cold cavity, and (b) hot cavity environments. Both model runs use a commonly-used $C_D = 0.003$. Both ice shelves display melting over much of the ice shelf–ocean interface, while the refreezing area is much larger in the cold cavity.

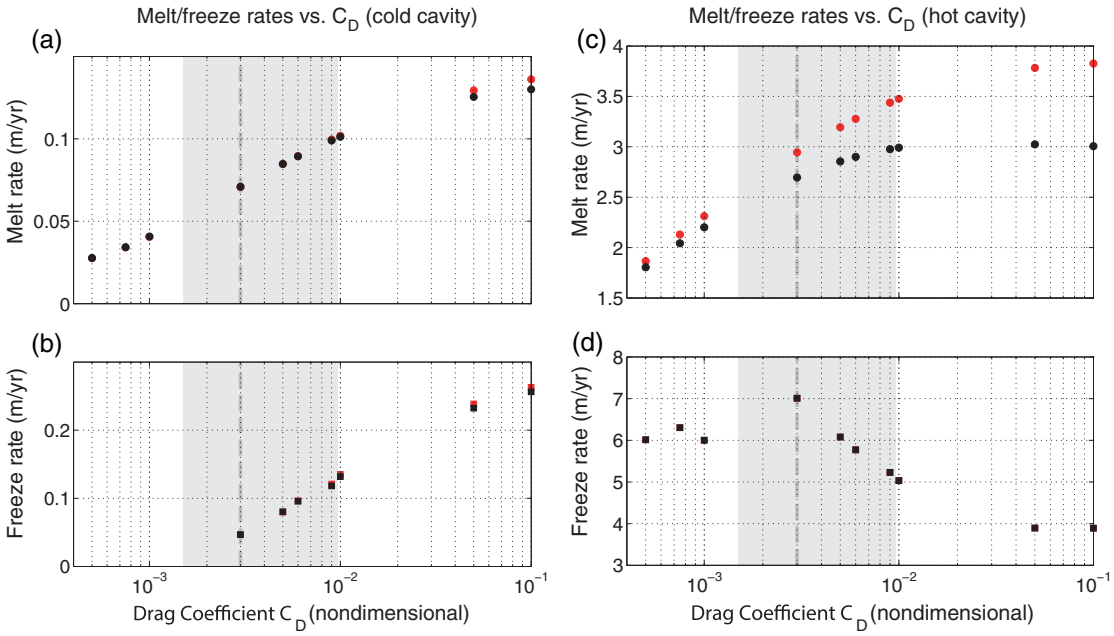

Fig. 5. Area averaged (a) melting and (b) freezing for the cold cavity environment and area averaged (c) melting and (d) freezing in the hot cavity environment are shown plotted against the drag coefficient beneath the ice shelf. The average melt and freeze rates are calculated only over the regions of melting and freezing, respectively. Black markers represent averages with the ice shelf front neglected from the average, while red markers include the ice front. Included is a shaded band indicating the range of C_D from literature and a commonly used value $C_D = 0.003$. (For interpretation of the references to colour in this figure legend, the reader is referred to the web version of this article).

created by cold meltwater ascending to where it is below the pressure dependent in situ freezing point and thus refreezing. The outflow region is also characterised by strong buoyancy-driven velocities enhancing rates of freezing. The pattern of refreezing along the western side of the ice shelf, where cold meltwater outflow is concentrated, has been observed on Antarctic ice shelves (e.g. Fricker et al., 2001). While refreezing occurs in the hot cavity simulations, we note that it occurs over a very small area. Furthermore, in the idealised hot cavity simulations, the buoyant melt water plume has a long distance over which to lose heat to the ice shelf. In reality, hot cavity ice shelves, which are smaller than that simulated here, may not exhibit refreezing.

In Fig. 5, the area-averaged melt/freeze rate, calculated from a temporal average of the last year of the model run, is shown as a function of the ice shelf–ocean interface drag coefficient. The area-average melt/freeze rate (positive for melting; negative for freezing) is calculated only across the area experiencing melting and freezing respectively. This allows properties of the ice shelf–ocean interaction to be investigated for both the melting and freezing areas separately, which is more important for the cold cavity scenario, where the area of refreezing is significant (Fig. 4(a)).

As expected, the cold cavity scenario, with colder and less saline surface forcing, leads to lower area averaged melt rates than the hot cavity environment (compare Fig. 5(a)–(c)). Melt increases monotonically with C_D, and begins to flatten as C_D increases to high values. Refreezing, which only occurs at moderate to high C_D, increases in magnitude as C_D increases in Fig. 5(b).

Results from the hot cavity scenario, where surface forcing is warmer and more saline, are shown in Fig. 5(c and d). Melt rates are much higher than the cold cavity scenario; there is more melting at the ice front; and, melting reaches a peak value at lower C_D. Melting is weak for the lowest drag ($C_D < 1 \times 10^{-3}$), increases to a local maximum at moderate to high drag ($C_D = 1 \times 10^{-2}$), then plateaus above $C_D = 5 \times 10^{-2}$. Melting decreases marginally between $C_D = 5 \times 10^{-2}$ and $C_D = 1 \times 10^{-1}$.

Refreezing in the hot cavity scenario is present in these idealised simulations, as shown in Fig. 5(d). The freezing in these scenarios is higher in magnitude than in the cold cavity scenario, but shows

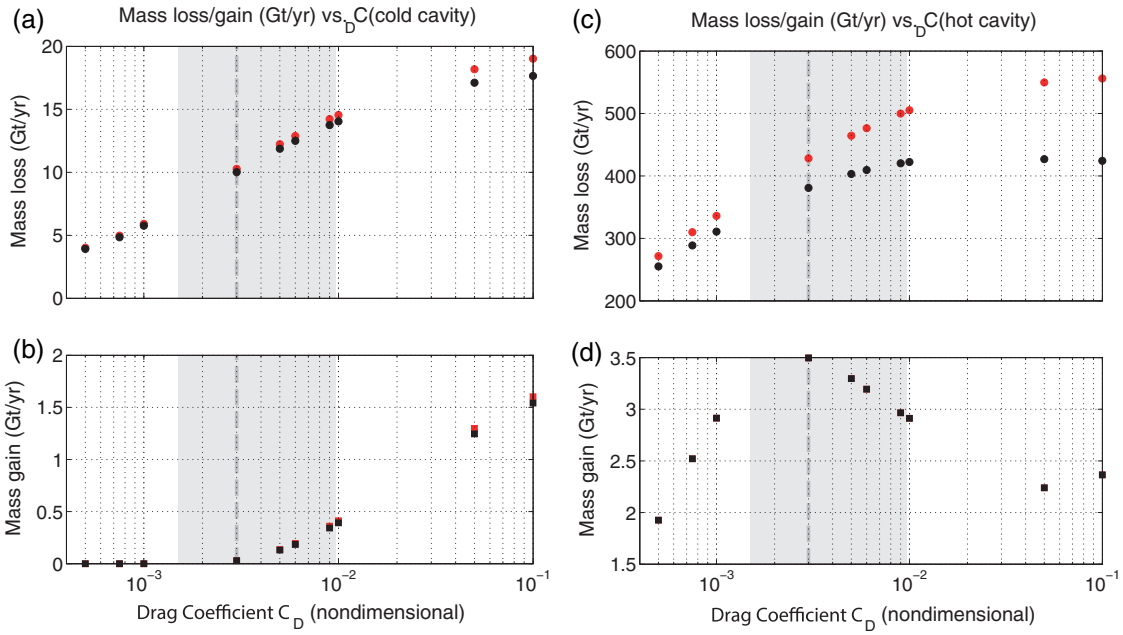

Fig. 6. The annual (a and c) mass loss and (b and d) mass gain are calculated for the areas displaying melting and freezing, respectively. This is calculated for both the (a and b) cold cavity conditions and (c and d) hot cavity conditions. Black markers represent averages with the ice shelf front neglected from the average, while red markers include the ice front. Shaded band indicates range of C_D from literature and vertical line is $C_D = 0.003$. (For interpretation of the references to colour in this figure legend, the reader is referred to the web version of this article).

a tendency to fluctuate in magnitude between different C_D. This is likely due to refreezing occurring over a small proportion of ice shelf area (0.2% for the lowest C_D tested increasing to 0.45% at the highest C_D tested; 4–8 model cells), making it more susceptible to noise as cells switch from freezing to melting. In the cold cavity, refreezing occurs over a larger area and hence monotonically increases in magnitude.

The melting and freezing weighted by the area of each process is shown by considering the integrated mass loss, calculated as $\Delta M = \rho_{ice} \int m(A) \cdot dA$, where m is the melt rate, A is the area of melting/freezing, ρ_{ice} is the density of ice, shown plotted for different C_D in Fig. 6. In each case, the trend in mass loss/gain is the same as the melt/freeze rate but the scaling by the area of each process weights the processes and allows them to be compared.

In the cold cavity scenario, Fig. 6(a–b), mass loss increases with increasing C_D. Mass gain through refreezing is a low proportion of mass loss (1–10%), though it increases for increasing C_D. The mass loss in the hot cavity scenario (Fig. 6(c)) follows the same trend as the hot cavity melt rate, increasing with increasing C_D before plateauing for moderate to high C_D. The mass gain through freezing is a tiny fraction of the mass loss (<1%), showing that the high average freeze rate in Fig. 5(d) should be treated as a small contribution to the thermodynamic interaction in the hot cavity environment. Furthermore, the cold cavity mass loss is approximately 1–4% of the hot cavity mass loss while the cold cavity mass gain is approximately 7–17% of the hot cavity mass gain for moderate drag, increasing to 55–63% for high drag.

The thermal driving across the ice shelf–ocean interface is calculated as $T_* = T_M - T_B - a(S_M - S_B)$, which accounts for a temperature and salinity difference from the top model cell to the interface. Here, a is the salinity coefficient of the linearised freezing equation (see Eq. A.1). A positive thermal driving indicates heat available for melting, while a negative thermal driving indicates supercooling and the potential for refreezing.

For the cold cavity, thermal driving is low for the melting region, and decreasing for increasing C_D (Fig. 7(a)). In the refreeze zone, the thermal driving is negative and is increasing in magnitude as C_D is increased as (Fig. 7(b)). The thermal driving in the hot cavity is significantly stronger than the cold cavity ($T_* \approx 1$°C for low drag) and decreases with increasing C_D. In the refreeze zone, thermal driving is negative, and in contrast to the cold cavity refreeze zone, decreases with increasing C_D. The maximum magnitude of negative thermal driving in the refreeze zone is much higher ($T_* = -0.45$°C) and occurs at the lowest C_D, compared to the maximum magnitude of thermal driving in the cold cavity scenario ($T_* = -0.0018$°C), which occurs at the highest C_D. Note that in reality, the degree of supercooling observed in the hot cavity at low drag would be quenched by the formation of frazil crystals within the water column, which is an effect not included in these model runs. The behaviour of T_* with C_D for the refreezing areas, is increasing in magnitude for the cold cavity and decreasing in magnitude for the hot cavity. This inversion, visible in the freeze rate behaviour of the refreezing zones, is discussed in Section 5.1.

Velocity near the ice shelf–ocean interface is investigated with top layer velocity magnitude $|U_M|$ and friction velocity u_* (Fig. 8). These have complementary but different uses for diagnosing how velocity affects melting; u_* feeds directly into the three equation parameterisation, so understanding this is important for understanding the thermodynamics of the three-equation parameterisation; and, $|U_M|$ is the physical realisation of flow across the ice face and as a result shows the effect of drag.

For a cold cavity, the boundary layer velocity magnitude ($|U_M|$; Fig. 8(a)) increases for increasing C_D, except at high C_D, where there is a decrease in $|U_M|$ for the melt region after peaking at $C_D \sim 2 \times 10^{-2}$. The area-averaged friction velocity, u_* displays increasing magnitude with increasing C_D for both the melting and freezing regions.

The hot cavity scenario displays similar behaviour to the cold cavity scenario, but u_* and $|U_M|$ are now an order of magnitude higher. The maximum $|U_M|$ occurs in the hot cavity scenario at lower drag ($C_D = 0.003$) than in the cold cavity scenario ($C_D \approx 0.01$).

4.2. Friction-driven turbulence and velocity dependent/independent melting

Here, the contribution to the melt rate from the impact of C_D on both the heat flux into the ice and by driving mixing into the

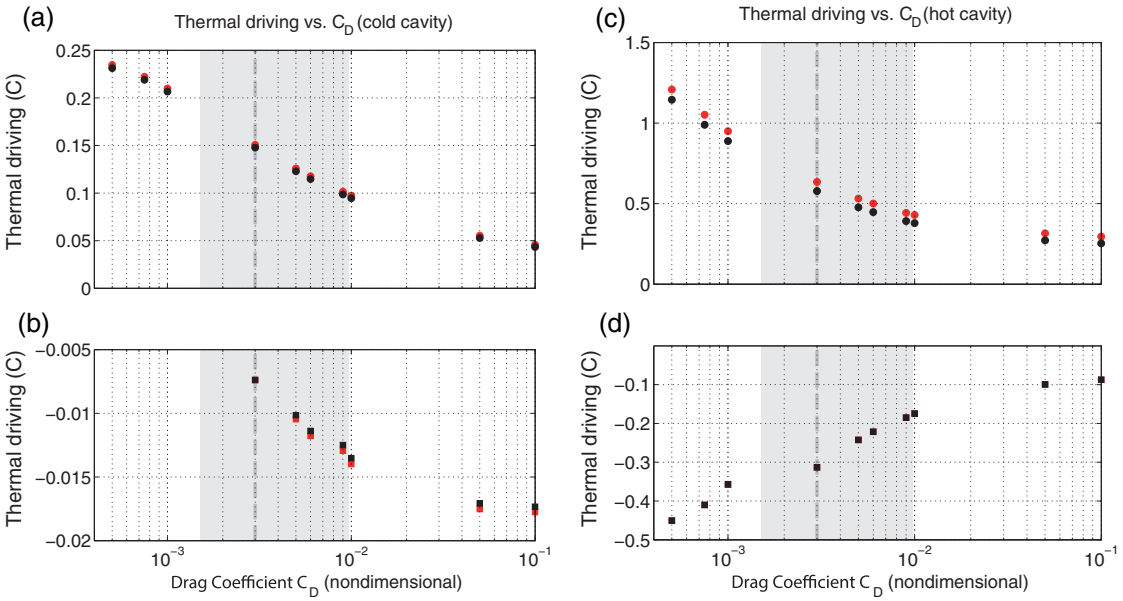

Fig. 7. The area-averaged thermal driving, $T_* = T_M - T_B - a(S_M - S_B)$ for the (a and c) melting and (b and d) freezing regions, for different basal roughness. This is shown for both the (a and b) cold cavity and (c and d) hot cavity conditions. Black markers represent averages with the ice shelf front neglected from the average, while red markers include the ice front. Shaded band indicates range of C_D from literature and vertical line is $C_D = 0.003$. (For interpretation of the references to colour in this figure legend, the reader is referred to the web version of this article).

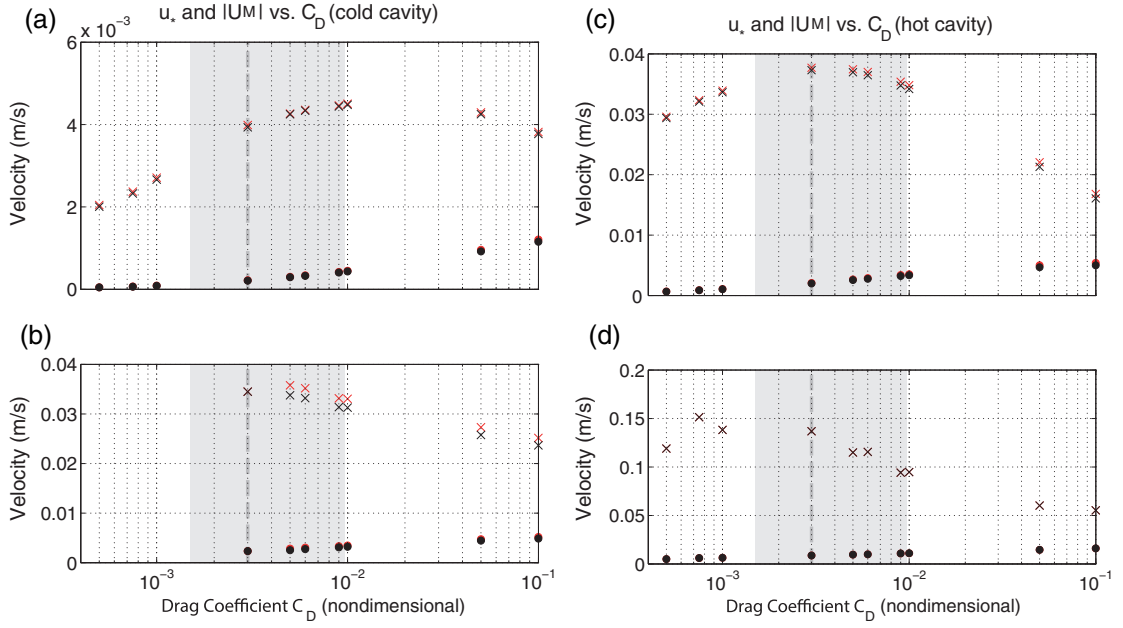

Fig. 8. The area-average boundary layer velocity magnitude ($|U_M|$; crosses) and the area-average friction velocity (u_*; circles) are plotted. The area-average velocity magnitude is calculated from the model layers which fall within the surface boundary layer as calculated by the surface mixing parameterisation. This is shown for the (a and c) melt regions and the (b and d) freeze regions and was calculated for (a and b) cold cavity and (c and d) hot cavity conditions. Black markers represent averages with the ice shelf front neglected from the average, red markers include the ice front. Shaded band indicates range of C_D from literature and vertical line is $C_D = 0.003$. (For interpretation of the references to colour in this figure legend, the reader is referred to the web version of this article).

boundary layer is investigated by selectively turning off these effects. Note that since holding $\gamma_{T|S}$ constant is a much larger effect than removing friction-driven turbulent mixing, results of case (c) and case (d) are similar and thus we do not show the results of case (d). We also found the hot environment, high drag simulations run without friction-driven turbulent mixing were subject to instabilities above $C_D = 0.05$. Hence, the high drag sensitivity studies use $C_D = 0.1$ for the cold cavity and $C_D = 0.05$ for the hot cavity.

Fig. 9 shows results of the first sensitivity study (case b), which investigated the effect of removing friction-driven turbulent mixing. Fig. 9(a, c, e and g) show the spatial distribution of melting and freezing (m/yr), while Fig. 9(b, d, f and h) show the melt quotient (melt rate of the sensitivity study divided by the melt rate of the control run; nondimensional). Fig. 9(a–d) show the low drag interface ($C_D = 0.0005$), while Fig. 9(e–h) show the results of the high drag interface ($C_D = 0.1$ for Fig. 9(e and f); $C_D = 0.05$ for Fig. 9(g and h)). The first two rows (Fig. 9(a, b, e and f) are for the cold cavity, and the third and fourth rows (Fig. 9(c, d, g and h) are for the hot cavity.

For the low drag ($C_D = 0.0005$), cold cavity runs (Fig. 9(a and b)), the effect of no frictional mixing is a minor (<5%) decrease in melt

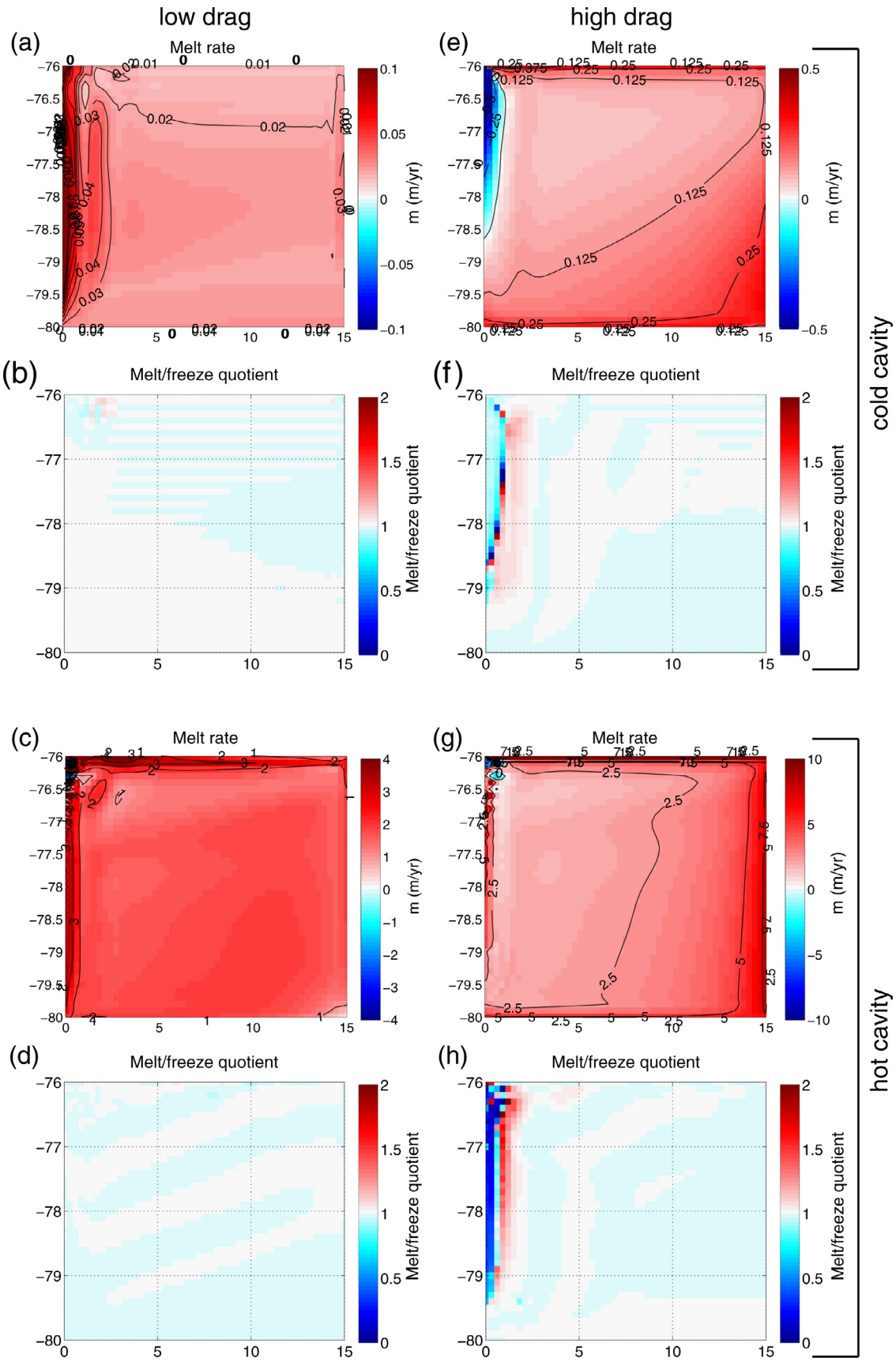

Fig. 9. Melt rate (a, c, e and g; m) plotted for the control run (with friction-driven turbulent mixing), and fractional change in melt rate (b, d, f and h; $m_{noFDTM}/m_{withFDTM}$) plotted for the sensitivity studies without friction-driven turbulent mixing. (a–d) are low drag ($C_D = 0.0005$) and (e–h) are high drag ($C_D = 0.1$ for (e and f); $C_D = 0.05$ for (g and h)). Panels (a and b) and (e and f) are cold cavity environments, while (c and d) and (g and h) are hot cavity environments. Changes in sign (e.g. freezing changing to melting) will saturate the colour scale of $m_{noFDTM}/m_{withFDTM}$, which is not shown as the number of cells which change from melting to freezing is small.

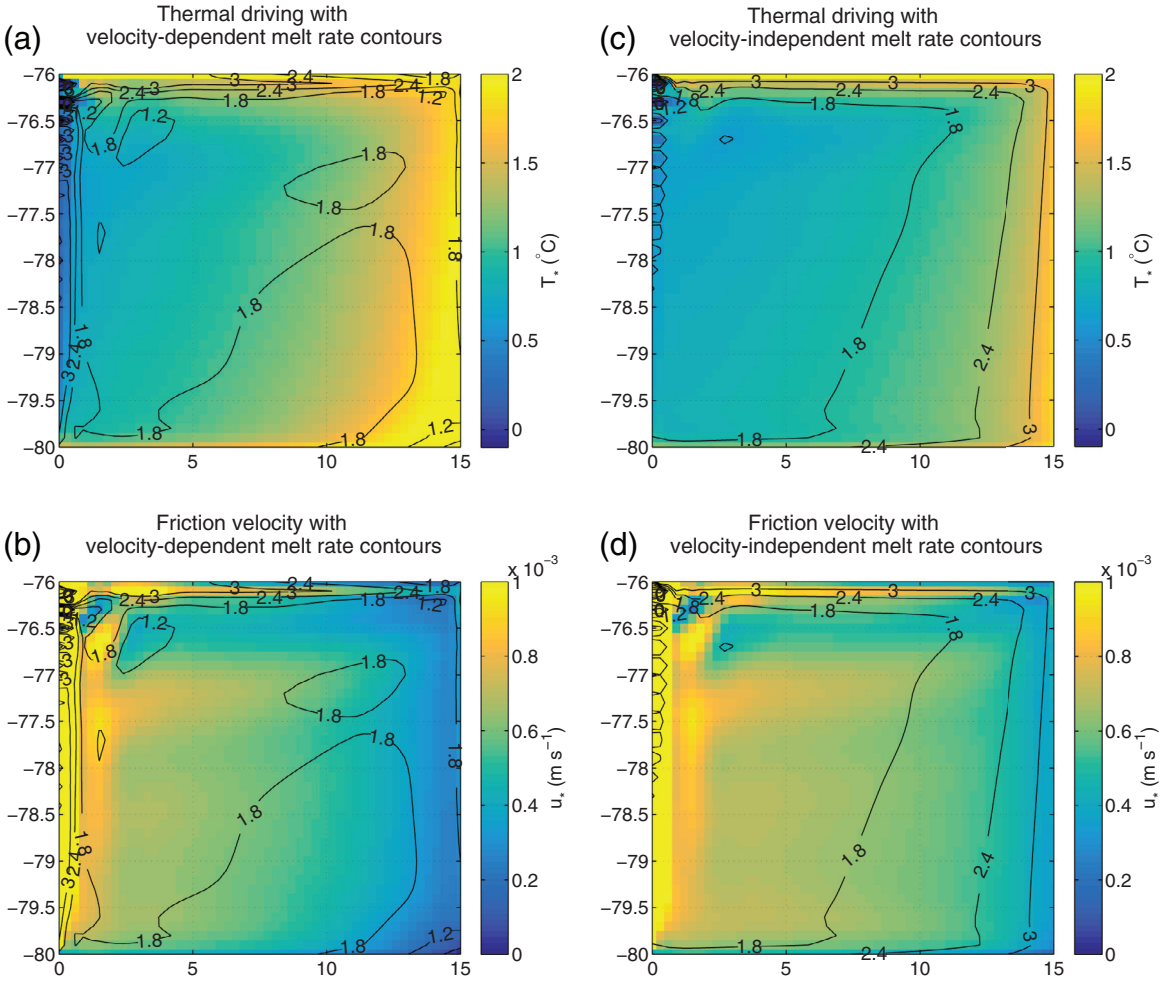

Fig. 10. Thermal driving (a and c) and Friction velocity (b and d) plotted for the velocity-dependent control simulation (a and b) and the velocity-independent sensitivity study (c and d), with melt rate contours from the respective model run. These results are for the hot cavity environment with low drag ($C_D = 0.0005$).

across the front half of the ice shelf except along the shallow ice front region where melting is marginally increased (<5%).

In the high drag ($C_D = 0.1$), cold cavity runs (Fig. 9(e and f)), ignoring frictional mixing leads to strengthened refreezing, increased melting in the vicinity of the edge of the refreeze zone, and a widespread marginal decrease in melting.

In the low drag ($C_D = 0.0005$), hot cavity runs (Fig. 9(c and d)), the effect of the increased thermal driving is visible as relatively high melt rates (note the different colour scale between plotted melt rates), and a contracted refreeze zone, which consists of only a small number of cells. The effect of no frictional mixing is a widespread but weak decrease in melting.

In the high drag ($C_D = 0.05$), hot cavity sensitivity runs (Fig. 9(g and h)), the effect of no frictional mixing is strongly reduced melting along the western boundary, an adjacent band of strengthened melting and a widespread but weak decrease in melting.

The second sensitivity study (case c) tested the effect of velocity-independence in the melting parameterisation compared to the velocity-dependent control run (Fig. 10). This sensitivity study was conducted for the four driving conditions (cold cavity/low drag, cold cavity/high drag, hot cavity/low drag and hot cavity/high drag). However, results are presented only for the hot cavity/low drag study as it is representative of the results of the other studies. The thermal driving (top row) and friction velocity (bottom row) are plotted as colour maps with melt rate contours, where the first column is the velocity-dependent control run and the second column is the velocity-independent (i.e. constant $\gamma_{T/S}$) run.

Similar to Dansereau et al. (2014), we show the thermal driving and friction velocity for velocity-dependent and velocity-independent melting. In the case of velocity-dependent melting (Fig. 10(a and b)) there is strong correlation between m and u_* (Fig. 10(b)). Melting is between 1.2 and 1.8 m/yr for most of the ice shelf, including the eastern boundary where strong thermal driving exists (~2°C), indicating that melting is limited by turbulent exchange and u_*. The strongest melting (above 3 m/yr) exists along the western boundary, where strong outflow currents drive high u_*, despite the weak thermal driving (~0.5°C).

The velocity-independent melting study (Fig. 10(c and d)) shows melt rate contours aligned with thermal driving (Fig. 10(c)). Melting is strongest at the eastern boundary where T_* is ~2°C, and weakens towards zero at the western boundary. Friction velocity peaks along the western boundary (Fig. 10(d)), but as this sensitivity study enforces constant turbulent exchange velocities (independent of water velocity), melting does not increase along the western boundary.

4.3. Spatially- and temporally-varying drag

To test the effect of a dynamic (spatially- and temporally-varying) C_D field, two cases were run using a different C_D for melting and freezing cells. Since the freeze/melt boundary evolves with time, the C_D field is also temporally-varying.

To determine the effect of spatially- and temporally-varying C_D, the two runs with dynamic drag are compared against a control run with spatially-constant drag. The drag coefficients for the melt zones

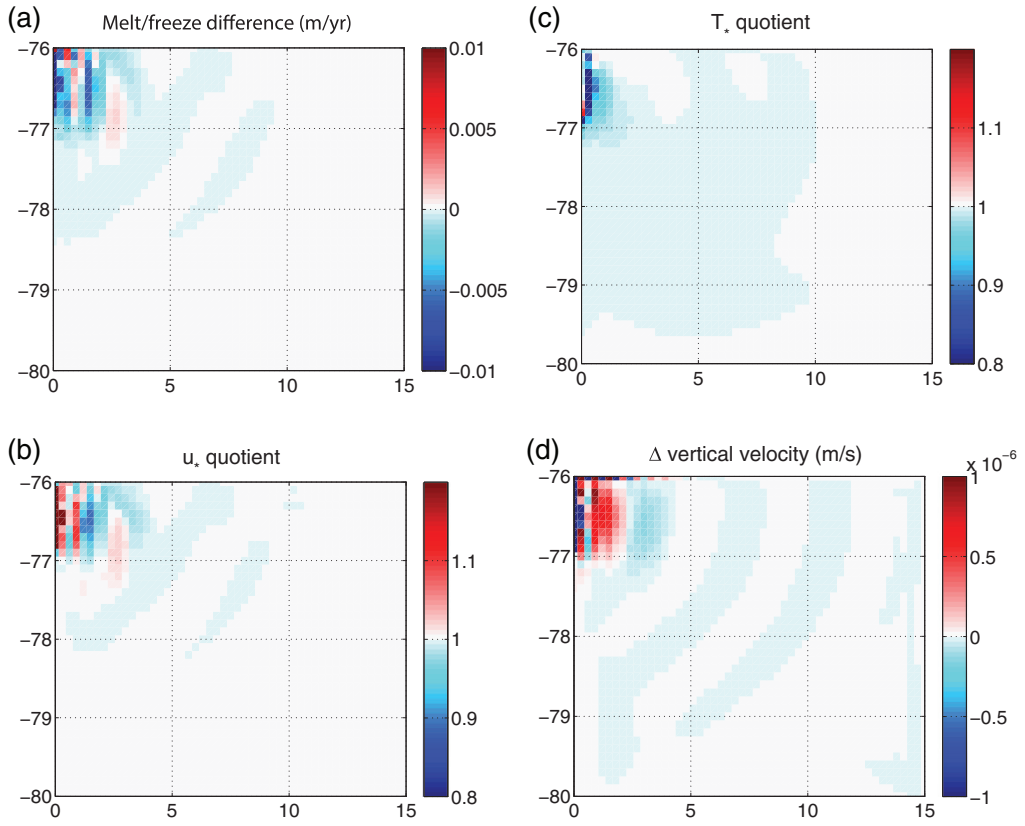

Fig. 11. The effect of spatially- and temporally-varying drag, with $C_{D,freeze} = 0.1$. (a) The difference in melt rate between the spatially-varying drag simulation and the spatially-constant drag simulation. A positive difference indicates stronger melting or weaker refreezing, and vice versa. (b) The quotient of u_* for the dynamic drag run divided by the spatially-constant drag run. A value greater than 1 indicates increased u_*. (c) The thermal driving (T_*) quotient, calculated as T_* for the dynamic drag run divided by T_* for the spatially-constant drag run. (d) The difference in vertical velocity into the top model layer between the dynamic drag and control run. A positive difference indicates increased vertical motion/upwelling.

of the sensitivity studies and the control run are chosen to be the same ($C_D = 0.003$) to allow comparison. Furthermore, this $C_{D,melt} = 0.003$ is chosen as it represents a moderate drag coefficient commonly used in the literature and thought to be physically representative for an ice interface not experiencing marine ice accretion. The cavity environment is chosen to be cold, in order to form a refreezing zone. The two dynamic drag models are similar but the results from the model with smoother refreeze zone $C_{D,freeze}$ are attenuated. As such, we report the results from the model with $C_{D,freeze} = 0.1$ and $C_{D,melt} = 0.003$ as it shows the largest difference in circulation and melt properties.

Comparing the melt/freeze distribution and magnitude between the control run (Fig. 4(a)) and the sensitivity studies (Fig. 11(a)), we see an increase in the rate of refreezing by 0.01 m/yr (~20%), while melting over the outflow region of the ice shelf decreased by 0.005–0.01 m/yr (~10%). There are two small zones of increased melting between the freeze zone and the ice shelf interior and at the ice shelf front. The area of refreezing increases by 25% (not shown).

The two contributing components to melt/freeze rates, u_* and T_*, also differ between the control runs and the dynamic drag runs. The friction velocity, Fig. 11(b), is generally similar across the ice shelf interior, but increases in the north-west of the ice shelf and adjacent to the freeze zone. Increased u_* is due to increased C_D over the freeze zone, but in the neighbouring melt region, where C_D is identical between the control and sensitivity runs, it indicates strengthened circulation. Thermal driving, T_*, is less for a majority of the ice shelf area as in Fig. 11(c). The strongest change in T_* is in the melt region adjacent to the refreeze zone where T_* is reduced by over 25%.

The difference in vertical flow into and out of the top model level displays significant changes, as in Fig. 11(d). There is increased downwards flow in the refreeze zone and a large adjacent area of upwards flow. From this area, a series of alternating downward then upward flow bands radiate south-east across the domain.

The spinup time for the constant drag and spatially-varying C_D simulations is approximately the same, meaning that temporal variation in C_D is of lesser importance. However, we expect that under non-steady-state forcing conditions (such as a seasonal cycle driving periodic refreezing), the temporal variation in C_D will be an important factor for changing melt dynamics.

5. Discussion

5.1. Thermal driving

Thermal driving, T_*, is calculated as the difference in temperature and salinity between the interface (at the in situ freezing point) and the top model cell, and so signifies the potential for ice shelf melting or freezing.

For the melt regions of both cold (Fig. 7(a)) and hot cavities (Fig. 7(c)), the greatest T_* occurs for lowest C_D and as C_D increases, T_* decreases. This behaviour at low to moderate C_D is explained by the more efficient transfer of heat from the ocean to the ice shelf base as C_D is increased. Increased heat transfer removes more heat from the boundary layer while strengthened melting produces more meltwater; both of which reduce T_*.

This behaviour continues with increasing C_D but begins to plateau at high drag, which can be explained because melting increases as C_D is increased. The increased meltwater production cools and freshens the boundary layer and reduces T_*, while at the same time, increasing C_D increases the efficiency with which heat is transferred to

the ice shelf base (as parameterised by γ_T). If this increases faster than heat is transferred from the interior ocean to the boundary layer, then T_* will also decrease. This demonstrates that at high C_D, turbulent mixing is less important than meltwater input and heat transfer to the ice shelf base, for the heat balance of the boundary layer.

The cold and hot cavity refreeze zones display inverted behaviour (Fig. 7(b) and (d), respectively). The magnitude of T_* increases with C_D in the cold cavity, while in the hot cavity, the magnitude of T_* decreases with increasing C_D. In the cold cavity, the production of meltwater below the surface freezing point can produce freezing along the western boundary where strong outflow exists (Fig. 4(a)). Increasing C_D increases meltwater production and hence negative thermal driving in the outflow zone, despite the increased vertical mixing of cool interior waters. This is in contrast to the hot cavity where increasing C_D leads to more mixing of hot interior water into the boundary layer (through turbulent and divergent entrainment). In the hot cavity, the thermal effect of mixing relatively hot interior waters (decreasing $|T_*|$ in the freeze zone) is greater than the effect of increased meltwater production (increasing $|T_*|$ in the freeze zone), leading to an overall decrease in $|T_*|$ with increasing C_D.

Comparing the refreezing between the two cavity environments (while considering the small area of refreezing in the hot cavity), the inverted behaviour suggests that thermal conditions of the interior cavity water are important for determining whether refreezing increases or decreases with C_D. In a hot cavity, higher melting leads to buoyancy driven currents, strong entrainment and vertical diffusion of relatively hot interior waters, and weakened refreezing at higher drag. In a cold cavity, weaker melting and buoyancy driven circulation reduces the importance of entrainment and diffusion of interior waters, which furthermore are cooler and less able to reduce refreezing at high drag.

5.2. Top layer velocities

For low to moderate drag, $|U_M|$ increases with C_D, showing the strengthening of the buoyancy-driven circulation. However, at high drag, $|U_M|$ decreases with increasing C_D, as the increasing surface roughness decelerates the water in the boundary layer (Fig. 8).

Despite u_* being a function of the boundary layer velocity through $u_* = \sqrt{C_D}|U_M|$, the effect of the decreasing $|U_M|$ is overcome by the increasing C_D. As a result, the friction velocity increases with increasing C_D. It is noteworthy that for high C_D in the hot cavity, u_* begins to plateau, because the high drag is significantly decelerating the boundary layer flow.

The presence of a maximum $|U_M|$ in both the cold and hot cavity environments indicates that deceleration of circulation due to increasing drag is stronger than the increased buoyancy-driven circulation at higher melt. The local maximum in $|U_M|$ occurs at a lower drag for the warmer cavity environment. This is possibly due to the relative contributions from the positive effect of increasing buoyancy driven circulation and the negative effect of deceleration from the rougher interface. In a hot cavity environment where melting is very strong even at low drag, melting will become less sensitive to increasing drag (see the change of slope of the melt rate with increasing drag in Fig. 5(c) vs. (a)) and hence the buoyancy driven circulation will no longer increase in strength with C_D, reaching an upper bound. In the hot cavity, the increase in buoyancy driven circulation is not as strong at low to moderate C_D, allowing the deceleration from increasing drag to decrease $|U_M|$. This is in contrast to the cold cavity, where buoyancy driven circulation is still strongly increasing until moderate to high C_D where the frictional effects become apparent. Assuming that the location of the local maximum in $|U_M|$ is due to the strength of the increase in buoyancy driven circulation, it follows that in a very hot cavity environment (i.e. warmer inflow waters than are simulated here), where buoyancy driven circulation is at a maximum at low drag, frictional effects will dominate and $|U_M|$ will begin to decrease at low C_D.

5.3. Melt rate

The increasing area-averaged melt rate with C_D for low to moderate C_D (Fig. 5) is consistent with heat flux which is proportional to the drag coefficient. While the lower interface friction should lead to fast boundary layer flow, the lower drag decreases the turbulent mixing of heat (and salt) at the ice shelf–ocean boundary necessary to increase melt rates. This behaviour is similar for both hot and cold cavity scenarios. As C_D is increased, turbulent mixing increases, driving stronger melting.

Theoretically, this is explained by m increasing with increasing turbulent exchange (Eq. 2). Since the turbulent exchange velocities, $\gamma_{T/S}$ increase with increasing u_* (Eq. A.4), and u_* increases with $\sqrt{C_D}$ (Eq. 1; assuming the decrease in $|U_M|$ is less than the increase in $\sqrt{C_D}$), so we might expect m to increase with increasing C_D.

As C_D reaches moderate to high values, the behaviour of m changes. This is most noticeable in the hot cavity as a plateauing in m for $C_D > 0.01$. While it is tempting to attribute this to the decreasing top layer velocity magnitude (due to increased drag), u_* is still increasing with C_D. Consequently, the maximum in m must be attributed to the low T_* at high C_D. Therefore, the local maximum in the m–C_D relationship indicates a transition from velocity driven-melting to heat limited-melting. In a cavity environment hotter than that simulated here, buoyant circulation would be strong at low C_D and the effect of increasing drag would occur at lower C_D. As a result, u_* would plateau at lower C_D and m would peak at lower C_D.

The range of choices for C_D, as quoted in the literature, falls on the flank of the local maximum of melting in both the hot and cold cavity scenarios. This indicates higher sensitivity of m to C_D than if the range of C_D choices had fallen on the local melt maxima. Assuming that the range of C_D represents an estimate of uncertainty in C_D, these results suggest a 25% (in the hot cavity) to 70% (in the cold cavity) change in melt rates across the range of uncertainty. In a cavity environment warmer than simulated here, the local melt maximum could fall within the range of commonly chosen C_D, leading to increased robustness to uncertainty in C_D.

Dansereau et al. (2014) investigated the difference in melt rate distribution between velocity-independent and velocity-dependent exchange coefficients, $\gamma_{T/S}$, for a situation similar to our hot cavity scenario and over approximately the same range of C_D. They found melting was controlled primarily by thermal driving in the velocity-independent case and by the strength of the boundary layer current in the velocity-dependent case. Their results agree with the relationship between melt rate and the low to moderate values of C_D used in this study (Sections 4.1 and 4.2). However, at high values of C_D, we encounter a decrease in m with increasing C_D, that occurs when the thermal driving continues to decrease while u plateaus. Dansereau et al. (2014) do not encounter a maximum C_D beyond which m decreases. The Dansereau et al. (2014) simulations are forced with hot inflowing water, which leads to stronger currents and higher melt rates than those produced in this study (Section 4.1). It may be that Dansereau et al. (2014) cannot separate the frictional deceleration due to the strength of the forced inflow. It is also unknown to what extent the vertical diffusion parameterisation (constant coefficients) of Dansereau et al. (2014) is limiting the simulation of a C_D-m maximum.

5.4. Frictional-driven turbulent mixing and velocity-dependent melting

The most pronounced effect of removing friction-driven turbulent mixing is the strengthening of melting along the edges of the refreeze zones and the subsequent contraction of the area of refreeze (Fig. 9).

This is present in the high drag simulations for both cavity environments, but is not present in either of the low drag simulations (which display zero or limited refreezing). It is likely that this constricted refreezing process occurs at any drag, as long as there is sufficient outflow and negative thermal driving to cause refreezing.

Other noticeable effects are decreased refreezing (in the models that display refreezing) of approximately 5%, and a widespread but weak decrease in melting.

These effects can be explained by the role that friction-driven turbulence has on mixing of heat and salt into the boundary layer. Turbulence created by basal roughness increases mixing of interior water into the boundary layer. In these experiments, the interior water is warmer and saltier than water close to the ice shelf, due to cold, fresh meltwater production. By removing the mixing of warmer interior waters into the boundary layer, melting is reduced. The reduction in freeze rates along the western boundary for both high drag scenarios can be explained by reduced meltwater production; and, reduced turbulent mixing leading to a thinner boundary layer. The contracting freeze zone is due to a strong increase in melting directly adjacent to the refreeze zone pushing westwards the negative thermal driving necessary for freezing. This zone of increased melt can be traced to strengthening of the sub-ice shelf recirculation, particularly along the western boundary.

The spatial pattern of melting and refreezing is shown to be strongly dependent on whether or not boundary layer velocity is included in the melting parameterisation. Model runs which use velocity-independent constant exchange coefficients ($\gamma_{T/S}$) display a melt distribution that is spatially correlated with the degree of thermal driving (see Losch, 2008). Model runs which implement exchange velocities that vary as a function of the currents (u_*) show a melt rate distribution which is principally correlated with the current field and the thermal driving to a lesser degree.

Dansereau et al. (2014) investigated the difference in melt rate distribution between velocity-independent and velocity-dependent exchange coefficients, $\gamma_{T/S}$, for a situation similar to our hot cavity scenario and over approximately the same range of C_D. They found melting was controlled primarily by thermal driving in the velocity-independent case and by the strength of the boundary layer current in the velocity-dependent case. Our study further supports results suggesting that melting will not necessarily be focussed where T_* is high (such as deep ice shelf grounding lines) but likely to be shifted to regions where strong flow past the ice shelf interface exists (Mueller et al., 2012; Dansereau et al., 2014), which motivates the inclusion of velocity-dependent turbulent exchange velocities (Jenkins et al., 2010). The similarity in our results to those of Dansereau et al. (2014), in spite of different lateral boundary forcing (closed lateral boundaries versus boundary inflow in Dansereau et al. (2014)) supports our choice of closed lateral boundaries and further reinforces the robustness of melting aligning with regions of strong flow.

5.5. Impact of spatially and temporally varying drag

The results from the dynamic drag experiment (Section 3.3) showed variation in the distribution and magnitude of melt rate (Fig. 11). The most important aspects are differences in melt rate distribution and magnitude, circulation and thermal driving which occur outside of the refreeze zone. Since the sensitivity and control studies use the same C_D for melt zones, any differences in the melt regions are a result of altered circulation and heat transport beneath the ice shelf. These differences have implications for ice shelf–ocean models which simulate substantial refreeze zones with the same C_D for both freezing and melting regions.

Freezing is increased in both magnitude and extent, in agreement with the results shown in Section 4.1 and discussed in Section 5.3. Changes to refreezing are due to increased drag leading to increased turbulent exchange velocities and increased flux across the ice shelf–ocean interface. However, the area of higher C_D is not large enough to significantly decelerate the general sub-ice shelf circulation.

Broad changes to U_M across the melt zone are a result of the increased refreezing driving stronger brine rejection, densification and overturning circulation. Increased densification in the refreeze zone changes horizontal pressure gradients and causes changes in horizontal circulation. Convergence and divergence resulting from the altered horizontal circulation then leads to downwelling and upwelling, respectively. A series of altered upwelling and downwelling bands form, radiating from this outflow region across the ice shelf. These bands of altered vertical velocity lead to a reorganisation of circulation along the ice shelf interface and drive stronger melting in two localised regions. The most important region of altered melting is the deeper band of increased melting (strongest at 77°S, 2.5°E), which produces more meltwater. The freshening and cooling effect of the increased melting leads to a swath of decreased T_* as the general circulation directs the meltwater to the north-west.

These results have important implications for ice shelf–ocean models and particularly those that utilise a single C_D for the entire ice shelf interface. Refreezing can be systematically underestimated, if C_D is spatially unchanging and chosen to best fit smooth, melt-dominant environments, as is often the case. Incorporating a C_D which is rougher for zones of refreezing will more realistically capture the sub-ice shelf environment in the presence of refreezing, leading to increased freeze rates. Furthermore, the effect of altered refreezing is not confined to the refreeze zone. Circulation patterns alter and reconfigure across the rest of the ice shelf, leading to significantly changed melting magnitude and distribution, motivating the importance of including distinct $C_{D,\,melt}$ and $C_{D,\,freeze}$.

Furthermore, these results provide strong motivation and support for the development of wide-scale geophysical observation techniques for basal roughness, similar to that demonstrated for detecting and quantifying surface-roughness elements from an airborne radar platform (e.g. Grima et al., 2014). Hydrographic measurements of turbulence beneath ice shelves will also be required to calibrate wide-scale roughness observations (e.g. Robinson et al., 2010; Stanton et al., 2013; Stevens et al., 2014).

6. Conclusions

Ice shelf basal melting is an important control on mass loss from Antarctica and hence the rate of sea level rise. Observations of basal melting and ocean state are difficult to achieve in situ, but can be readily simulated in numerical ocean models which capture the thermodynamic interaction of the ocean and ice shelves. We have run idealised ice shelf–ocean simulations, based on ROMS, with a commonly used parameterisation of ice–ocean thermodynamic interaction to investigate the effect of basal roughness on melting and freezing.

Melt rate increases with increasing C_D. However, we found that for a hot cavity environment, the rate of increase of melting plateaus for high C_D. It follows that for a very hot cavity scenario, melting will not increase and may even decrease with C_D. Friction velocity increases with increasing drag, even though water in the boundary layer is experiencing increasing deceleration from basal roughness. Increased friction velocity leads to increased exchange across the ice–ocean interface, and increased melting (and freezing). Increased melting produces more meltwater, and together with more efficient heat transfer from the boundary layer to the ice, thermal driving decreases with increased C_D. Beneath refreeze zones, the situation is more complicated. In the cold cavity, buoyancy driven circulation, entrainment and diffusion of cool interior waters into the boundary layer are a weaker effect than the increased meltwater production, leading to stronger negative thermal driving at high drag; in the hot cavity, buoyancy driven circulation is strong, entraining more warm

interior water into the boundary layer and reducing the negative thermal driving from meltwater.

Sensitivity studies showed that the effect of a vertical mixing scheme transporting heat into the boundary layer as a result of roughness at the ice–ocean interface is particularly important for capturing the magnitude and area of refreezing. Neglecting this effect, possibly through a poor or unresolved boundary layer scheme, can lead to underestimation of refreezing. Melting can be more dependent on the distribution of currents (u_*) rather than the distribution of thermal driving. This suggests that melting can be focussed in areas of strong flow rather than areas of solely strong thermal driving, so that melting may not be strongest at the deep grounding zones.

A drag coefficient that was larger for areas of refreezing and smaller for areas of melting led to variations in refreezing and melting across the entire ice shelf interface. Strengthened refreezing due to a rougher and more realistic C_D has implications for ice shelf–ocean models that simulate colder cavity ice shelves with substantial areas of refreezing. However, changes to melting across the entire ice shelf as a result of a spatially-varying C_D prompts the inclusion of a more realistic treatment of C_D for all ice shelf–ocean models. Ultimately, this would entail including a spatial distribution of basal roughness from observations, further motivating the continued development of wide-scale geophysical observations of basal roughness.

Future ice shelf–ocean model intercomparison projects and models may benefit from a standardised geometry and forcing that is modified to increase realism, such as with tidal forcing, different bathymetry or non-linearly sloped ice shelf draft. Furthermore, understanding of the role of large-scale roughness features, such as crevasses and inverted melt channels which act to constrain and modify melting (Dutrieux et al., 2014), would benefit through further investigation with idealised models (e.g. Gladish et al., 2012).

Lastly, we conclude that as model vertical resolution improves, it may be necessary to reformulate the standard practice for implementing the Holland and Jenkins (1999) ice–ocean thermodynamic parameterisation.

Acknowledgement

The authors would like to thank two anonymous reviewers and Malte Thoma for comments and suggestions that improved this manuscript. We also thank Craig Stevens for his comments and suggestions. This work was supported through the Australian Government's Cooperative Research Centre Programme through the Antarctic Climate & Ecosystems Cooperative Research Centre and through the Australian Research Council Special Research Initiative. David Gwyther is supported by the Australian Government CSIRO and University of Tasmania through the Quantitative Marine Science PhD program. Computing resources were provided by both the Tasmanian Partnership for Advanced Computing and the National Computational Infrastructure under grant m68.

Appendix A. 3-equation parameterisation

Thermodynamic interaction at the ice–ocean interface is not directly solved but must be parameterised via equations describing the in situ freezing temperature, and the heat and salt conservation at the interface. The most commonly used formulation for capturing thermodynamic interaction at the ice–ocean interface is the 3-equation parameterisation (Hellmer and Olbers, 1989; Scheduikat and Olbers, 1990; Holland and Jenkins, 1999). This is based on the following three equations:

$$T_B = aS_B + b + cp_B \tag{A.1}$$

$$Q^T_{latent} = Q^T_I - Q^T_M \tag{A.2}$$

$$Q^S_{brine} = Q^S_I - Q^S_M \tag{A.3}$$

Eq. A.1 defines the temperature of seawater film in contact with the base of the ice (T_B) to be at the local freezing point, calculated as a function of the in situ salinity, S_B and the in situ pressure, p_B. The constant coefficients are $a = -5.73 \times 10^{-2}$ °C, $b = 9.39 \times 10^{-2}$ °C and $c = 7.53 \times 10^{-8}$ °C Pa^{-1} (Holland and Jenkins, 1999). In Eq. A.2, the excess/deficit of heat flux at the interface (the heat flux conducted into the ice shelf, Q^T_I, minus the heat flux diffused to the interface from the log layer below, Q^T_M) is balanced by latent heat absorbed/released due to melting/freezing, Q^T_{latent}. By analogy, Eq. A.3 describes the brine flux Q^S_{brine} required to maintain the interface salinity during melting and freezing as the difference between diffusive salt flux in the ice, Q^S_I, and diffusive salt flux to the interface, Q^S_M. Following Holland and Jenkins (1999), diffusion of salt into the ice shelf is considered to be null ($Q^S_I = 0$). A schematic of these properties are shown in Fig. 2.

Both the latent heat (Q^T_{latent}) and brine flux (Q^S_{brine}) are a function of a melt/freeze rate, which is defined as a thickness of ice melted (or frozen) per unit time. Likewise, the heat and salt fluxes to the interface (Q^T_M and Q^S_M respectively) vary with the temperature difference and salinity difference across the upper log layer. Furthermore, both heat and salt fluxes in the log layer are functions of the thermal exchange velocity, γ_T and the salinity exchange velocity γ_S, respectively.

Following others (Kader and Yaglom, 1972; McPhee et al., 1987; Holland and Jenkins, 1999), we define these exchange velocities, $\gamma_{T/S}$ in terms of the friction velocity, u_*, the turbulent transfer parameter Γ_{turb} and the molecular transfer parameter $\Gamma^{T/S}_{mole}$,

$$\gamma_{T/S} = \frac{u_*}{\Gamma_{turb} + \Gamma^{T/S}_{mole}}, \tag{A.4}$$

where, the contribution from molecular diffusion,

$$\Gamma^{T/S}_{mole} = 12.5(Pr, Sc)^{2/3} - 6, \tag{A.5}$$

is related to the Prandtl number ($Pr = 13.8$; ratio of viscosity to thermal diffusivity) for thermal diffusion (Γ^T_{mole}) and the Schmidt number ($Sc = 2432$; ratio of viscosity to saline diffusivity) for saline diffusion (Γ^S_{mole}). The turbulent transfer coefficient is given by

$$\Gamma_{turb} = \frac{1}{\kappa} \ln\left(\frac{u_* \xi_N \eta_*^2}{f h_\nu}\right) + \frac{1}{2\xi_N \eta_*} - \frac{1}{\kappa}, \tag{A.6}$$

where h_ν is the viscous sublayer thickness, $\xi_N = 0.052$ is a dimensionless stability constant, η_* is the stability parameter, Von Kármán's constant is $\kappa = 0.40$ and f is the coriolis parameter (See Holland and Jenkins, 1999, for full parameterisation details).

References

Cougnon, E.A., Galton-Fenzi, B.K., Meijers, A.J.S., Legrésy, B., 2013. Modeling interannual dense shelf water export in the region of the Mertz Glacier Tongue (1992–2007). J. Geophys. Res. Oceans 118, 5858–5872. doi:10.1002/2013JC008790.

Craven, M., Allison, I., Fricker, H.A., Warner, R., 2009. Properties of a marine ice layer under the Amery Ice Shelf, East Antarctica. J. Glaciol. 55 (192), 717–728. doi:10.3189/002214309789470941.

Dansereau, V., Heimbach, P., Losch, M., 2014. Simulation of subice shelf melt rates in a general circulation model: velocity-dependent transfer and the role of friction. J. Geophys. Res. Oceans 119 (3), 1765–1790. doi:10.1002/2013JC008846.

De Rydt, J., Holland, P.R., Dutrieux, P., Jenkins, A., 2014. Geometric and oceanographic controls on melting beneath Pine Island Glacier. J. Geophys. Res. Oceans 119 (4), 2420–2438. doi:10.1002/2013JC009513.

Depoorter, M.A., Bamber, J.L., Griggs, J.A., Lenaerts, J.T.M., Ligtenberg, S.R.M., van den Broeke, M.R., Moholdt, G., 2013. Calving fluxes and basal melt rates of Antarctic ice shelves.. Nature 502 (7469), 89–92. doi:10.1038/nature12567.

Dinniman, M.S., Klinck, J.M., Hofmann, E.E., 2012. Sensitivity of circumpolar deep water transport and ice shelf basal melt along the West Antarctic Peninsula to changes in the winds. J. Clim. 25 (14), 4799–4816. doi:10.1175/JCLI-D-11-00307.1.

Dinniman, M.S., Klinck, J.M., Smith, W.O., 2007. Influence of sea ice cover and icebergs on circulation and water mass formation in a numerical circulation model of the Ross Sea, Antarctica. J. Geophys. Res. 112, C11013. doi:10.1029/2006JC004036.

Dupont, T.K., Alley, R.B., 2005. Assessment of the importance of ice-shelf buttressing to ice-sheet flow. Geophys. Res. Lett. 32 (4), 1–4. doi:10.1029/2004GL022024.

Dutrieux, P., Stewart, C., Jenkins, A., Nicholls, K.W., Corr, H.F.J., Rignot, E., Steffen, K., 2014. Basal terraces on melting ice shelves. Geophys. Res. Lett. 41, 5506–5513. doi:10.1002/2014GL060618.

Fricker, H.A., Popov, S., Allison, I., Young, N., 2001. Distribution of marine ice beneath the Amery ice shelf. Geophys. Res. Lett. 28 (11), 2241. doi:10.1029/2000GL012461.

Galton-fenzi, B.K., 2009. Modelling Ice-Shelf/Ocean Interaction. Ph.D. thesis, University of Tasmania.

Galton-Fenzi, B.K., Hunter, J.R., Coleman, R., Marsland, S.J., Warner, R.C., 2012. Modeling the basal melting and marine ice accretion of the Amery Ice Shelf. J. Geophys. Res. 117, C09031. doi:10.1029/2012JC008214.

Gladish, C.V., Holland, D.M., Holland, P.R., Price, S.F., 2012. Ice-shelf basal channels in a coupled ice/ocean model. J. Glaciol. 58 (212), 1227–1244. doi:10.3189/2012JoG12J003.

Greene, C.A., Bliss, A.K., Blankenship, D.D., 2013. A Bedmap2 Toolbox for Matlab. In: American Geophysical Union Fall Meeting 2013. American Geophysical Union, pp. C51A–0495.

Grima, C., Schroeder, D.M., Blankenship, D.D., Young, D.A., 2014. Planetary landing-zone reconnaissance using ice-penetrating radar data: concept validation in Antarctica. Planet. Space Sci. 103, 191–204. doi:10.1016/j.pss.2014.07.018.

Gwyther, D.E., Galton-Fenzi, B.K., Hunter, J.R., Roberts, J.L., 2014. Simulated melt rates for the Totten and Dalton ice shelves. Ocean Sci. 10 (3), 267–279. doi:10.5194/os-10-267-2014.

Hattermann, T., Smedsrud, L., Nøst, O., Lilly, J., Galton-Fenzi, B., 2014. Eddy-resolving simulations of the Fimbul Ice Shelf cavity circulation: basal melting and exchange with open ocean. Ocean Model. 82, 28–44. doi:10.1016/j.ocemod.2014.07.004.

Hellmer, H.H., Kauker, F., Timmermann, R., Determann, J., Rae, J., 2012. Twenty-first-century warming of a large Antarctic ice-shelf cavity by a redirected coastal current. Nature 485 (7397), 225–228. doi:10.1038/nature11064.

Hellmer, H.H., Olbers, D.J., 1989. A two-dimensional model for the thermohaline circulation under an ice shelf. Antarct. Sci. 1 (4), 325–336.

Herraiz-Borreguero, L., Allison, I., Craven, M., Nicholls, K.W., Rosenberg, M.A., 2013. Ice shelf/ocean interactions under the Amery Ice Shelf: seasonal variability and its effect on marine ice formation. J. Geophys. Res. Oceans 118, 7117–7131. doi:10.1002/2013JC009158.

Holland, D.M., Jenkins, A., 1999. Modeling thermodynamic ice–ocean interactions at the base of an ice shelf. J. Phys. Oceanogr. 29 (8), 1787–1800. doi:10.1175/1520-0485(1999)029⟨1787:MTIOIA⟩2.0.CO;2.

Holland, D.M., Jenkins, A., 2001. Adaptation of an isopycnic coordinate ocean model for the study of circulation beneath ice shelves. Mon. Weather Rev. 129 (8), 1905–1927. doi:10.1175/1520-0493(2001)129⟨1905:AOAICO⟩2.0.CO;2.

Holland, P.R., Jenkins, A., Holland, D.M., 2008. The response of ice shelf basal melting to variations in ocean temperature. J. Clim. 21 (11), 2558–2572. doi:10.1175/2007JCLI1909.1.

Holland, P.R., Jenkins, A., Holland, D.M., 2010. Ice and ocean processes in the Bellingshausen Sea, Antarctica. J. Geophys. Res. 115, C05020. doi:10.1029/2008JC005219.

Hunter, J.R., 2006. Specification for Test Models of Ice Shelf Cavities. Technical Report June. Antarctic Climate & Ecosystems Cooperative Research Centre.

Jacobs, S.S., Jenkins, A., Giulivi, C.F., Dutrieux, P., 2011. Stronger ocean circulation and increased melting under Pine Island Glacier ice shelf. Nature Geosci. 4 (8), 519–523. doi:10.1038/ngeo1188.

Jenkins, A., Nicholls, K.W., Corr, H.F.J., 2010. Observation and parameterization of ablation at the Base of Ronne Ice Shelf, Antarctica. J. Phys. Oceanogr. 40 (10), 2298–2312. doi:10.1175/2010JPO4317.1.

Joughin, I., Alley, R.B., Holland, D.M., 2012. Ice-sheet response to oceanic forcing. Science 338 (6111), 1172–1176. doi:10.1126/science.1226481.

Kader, B., Yaglom, A., 1972. Heat and mass transfer laws for fully turbulent wall flows. Int. J. Heat Mass Transf. 15 (12), 2329–2351. doi:10.1016/0017-9310(72)90131-7.

Klinck, J.M., Dinniman, M.S., 2010. Exchange across the shelf break at high southern latitudes. Ocean Sci. 6 (2), 513–524. doi:10.5194/os-6-513-2010.

Large, W.G., McWilliams, J.C., Doney, S.C., 1994. Oceanic vertical mixing: a review and a model with a nonlocal boundary layer parameterization. Rev. Geophys. 32 (4), 363. doi:10.1029/94RG01872.

Lewis, E.L., Perkin, R.G., 1986. Ice pumps and their rates. J. Geophys. Res. 91 (C10), 11756–11762. doi:10.1029/JC091iC10p11756.

Little, C.M., Gnanadesikan, A., Oppenheimer, M., 2009. How ice shelf morphology controls basal melting. J. Geophys. Res. 114, C12007. doi:10.1029/2008JC005197.

Losch, M., 2008. Modeling ice shelf cavities in a z coordinate ocean general circulation model. J. Geophys. Res. Oceans 113, C08043. doi:10.1029/2007JC004368.

McPhee, M., 1992. Turbulent heat flux in the upper ocean under sea ice. J. Geophys. Res. 97, 5365–5379.

McPhee, M.G., Maykut, G.A., Morison, J.H., 1987. Dynamics and thermodynamics of the ice/upper ocean system in the marginal ice zone of the Greenland Sea. J. Geophys. Res. 92, 7017–7031. doi:10.1029/JC092iC07p07017.

Millgate, T., Holland, P.R., Jenkins, A., Johnson, H.L., 2013. The effect of basal channels on oceanic ice-shelf melting. J. Geophys. Res. Oceans 118, 6951–6964. doi:10.1002/2013JC009402.

Mueller, R.D., Padman, L., Dinniman, M.S., Erofeeva, S.Y., Fricker, H.A., King, M.A., 2012. Impact of tide-topography interactions on basal melting of Larsen C Ice Shelf, Antarctica. J. Geophys. Res. 117, C05005. doi:10.1029/2011JC007263.

Paterson, W.S.B., 2002. The Physics of Glaciers, 3rd edition Butterworth-Heinemann.

Pritchard, H.D., Ligtenberg, S.R.M., Fricker, H.A., Vaughan, D.G., van den Broeke, M.R., Padman, L., 2012. Antarctic ice-sheet loss driven by basal melting of ice shelves. Nature 484 (7395), 502–505. doi:10.1038/nature10968.

Robinson, N.J., Williams, M.J.M., Barrett, P.J., Pyne, A.R., 2010. Observations of flow and ice-ocean interaction beneath the McMurdo Ice Shelf, Antarctica. J. Geophys. Res. Oceans 115, C03025. doi:10.1029/2008JC005255.

Scambos, T.A., Haran, T.M., Fahnestock, M.A., Painter, T.H., Bohlander, J., 2007. MODIS-based Mosaic of Antarctica (MOA) data sets: continent-wide surface morphology and snow grain size. Remote Sens. Environ. 111 (2), 242–257. doi:10.1016/j.rse.2006.12.020.

Scheduikat, M., Olbers, D., 1990. A one-dimensional mixed layer model beneath the ross ice shelf with tidally induced vertical mixing. Antarct. Sci. 2 (1), 29–42. doi:10.1017/S0954102090000049.

Shchepetkin, A.F., McWilliams, J.C., 2005. The regional oceanic modeling system (ROMS): a split-explicit, free-surface, topography-following-coordinate oceanic model. Ocean Model. 9 (4), 347–404. doi:10.1016/j.ocemod.2004.08.002.

Soulsby, R.L., 1983. The bottom boundary layer of shelf seas. In: Johns, B. (Ed.), Physical Oceanography of Coastal and Shelf Seas. Elsevier Science Publishers B.V., Amsterdam, pp. 189–266.

St-Laurent, P., Klinck, J.M., Dinniman, M.S., 2013. On the role of coastal troughs in the circulation of warm circumpolar deep water on Antarctic Shelves. J. Phys. Oceanogr. 43 (1), 51–64. doi:10.1175/JPO-D-11-0237.1.

Stanton, T.P., Shaw, W.J., Truffer, M., Corr, H.F.J., Peters, L.E., Riverman, K.L., Bindschadler, R., Holland, D.M., Anandakrishnan, S., 2013. Channelized ice melting in the ocean boundary layer beneath Pine Island Glacier, Antarctica. Science 341 (6151), 1236–1239. doi:10.1126/science.1239373. (New York, N.Y.)

Steele, M., Mellor, G.L., McPhee, M.G., 1989. Role of the molecular sublayer in the melting or freezing of sea ice. J. Phys. Oceanogr. 19, 139–147. doi:10.1175/1520-0485(1989)019⟨0139:ROTMSI⟩2.0.CO;2.

Stevens, C., McPhee, M., Forrest, A., Leonard, G., Stanton, T., Haskell, T., 2014. The influence of an Antarctic glacier tongue on near-field ocean circulation and mixing. J. Geophys. Res. Oceans 119, 2344–2362. doi:10.1002/2013JC009070.

Timmermann, R., 2002. Simulations of ice-ocean dynamics in the Weddell Sea 1. Model configuration and validation. J. Geophys. Res. 107 (C3), 1–11. doi:10.1029/2000JC000741.

Warner, R.C., Roberts, J.L., 2013. Pine Island Glacier (Antarctica) velocities from Landsat7 images between 2001 and 2011: FFT-based image correlation for images with data gaps. J. Glaciol. 59 (215), 571–582. doi:10.3189/2013JoG12J113.